A&A 581, A93 (2015)
DOI: 10.1051/0004-6361/201526846

Astronomy & Astrophysics

The stability of the optical flux variation gradient for 3C 120⋆ *(Research Note)*

Michael Ramolla[1], Francisco Pozo Nuñez[1], Christian Westhues[1], Martin Haas[1], and Rolf Chini[1,2]

[1] Astronomisches Institut, Ruhr–Universität Bochum, Universitätsstraße 150, 44801 Bochum, Germany
e-mail: ramolla@astro.rub.de
[2] Instituto de Astronomía, Universidad Católica del Norte, Avenida Angamos 0610, Casilla 1280 Antofagasta, Chile

Received 29 June 2015 / Accepted 6 August 2015

ABSTRACT

New *B*- and *V*-band monitoring in 2014–2015 reveals that the Seyfert 1 Galaxy, 3C 120, has brightened by a magnitude of 1.4, compared to our campaign that took place in 2009–2010. This allowed us to check for the debated luminosity and time-dependent color variations claimed for SDSS quasars. For our 3C 120 data, we find that the B/V flux ratio of the variable component in the bright epoch is indistinguishable from the faint one. We do not find any color variability on different timescales ranging from about 1 to 1800 days. We suggest that the luminosity and time-dependent color variability is an artifact caused by analyzing the data in magnitudes instead of fluxes. The flux variation gradients of both epochs yield consistent estimates of the host galaxy contribution to our 7.″5 aperture. These results confirm that the optical flux variation gradient method works well for Seyfert galaxies.

Key words. galaxies: active – galaxies: Seyfert – galaxies: nuclei

1. Introduction

The UV to optical color ratio of the total AGN, measured in magnitude units, becomes bluer as the AGN brightens (e.g. Meusinger et al. 2011). Some studies attribute this change in color to the spectral hardening of the variable component (Giveon et al. 1999; Wilhite et al. 2005; Wamsteker et al. 1990; Webb & Malkan 2000). However, there is ample evidence to suggest that the color of the variable component stays constant and that the corresponding flux variation gradient is offset from the origin of the flux-flux diagram (Choloniewski 1981; Winkler et al. 1992; Winkler 1997; Paltani & Walter 1996; Sakata et al. 2010). In this case, the "bluer when brighter" total observed fluxes, which are measured in a finite aperture, are explained by the superimposition of a constant red host galaxy (including non-varying emission lines) and a varying blue AGN. Even if the measured host contribution is small, compared to the required offset of the flux variation gradient (FVG), there is no significant curvature seen in the flux-flux diagrams (Sakata et al. 2011).

The constancy of the optical colors of the variable component is physically plausible if the variable emission has a hot thermal origin, as expected for an accretion disk (AD). In this case, fluxes in the optical range lie on the Rayleigh-Jeans tail, and they scale almost linearly with temperature.

Recently, Sun et al. (2014) report time-dependent g/r color variability of the SDSS Stripe 82 quasar sample. A blue color at variations inside <30 days (with smaller amplitudes) gradually changes to redder colors on larger timescales >1000 days (and larger amplitudes). Furthermore, Sun et al. (2014) claim that the FVG method lacks rigor and is, therefore, not valid. Consequently, one also expects to find similar behavior for Seyfert galaxies, the less luminous siblings of quasars.

Using data from 2009–2010, Pozo Nuñez et al. (2012) performed *B*-, *V*-band monitoring of the Seyfert 1 Galaxy 3C 120 including dense daily observations over a period of five months. Here we report new *B*-, *V*-band results from a six-month monitoring project in 2014 and 2015. The total brightening (by about 1.4 mag) and the dense time-sampling of observations allow us to check whether or not brightness and time-dependent color variations are present.

2. Observations and data reduction

The new photometric data at Johnson *B* and *V* was observed between 27 August 2014 and 3 March 2015 at the Universitätssternwarte Bochum, near Cerro Armazones. We combined the RoBoTT telescope data (Pozo Nuñez et al. 2012) with new data from the BEST II (Kabath et al. 2009).

All data has been corrected for the latest revision of galactic foreground extinction[1] by Schlafly & Finkbeiner (2011) and the corresponding lightcurves are displayed in Figs.1 and 2.

3. Results

3.1. Flux-flux diagrams

Total *B*- versus *V*-band fluxes for the two epochs are shown in Fig. 3, with one that had low luminosity in 2009–2010 and one that had high luminosity in 2014–2015. Between the two epochs, the AGN luminosity increased by a magnitude of about 1.4 in both filters. The slope of AGN variability is well matched by a linear relation with $\Gamma_{BV} = 0.979 \pm 0.005$.

We consider the host colors of 3C 120 by Sakata et al. (2010) in a 8.″3 aperture, corrected for galactic foreground extinction (Schlafly & Finkbeiner 2011). Assuming that these will be similar when looked at in our 7.″5 aperture, this allows us to compute

⋆ Appendix A is available in electronic form at http://www.aanda.org

[1] $A_\lambda^B = 1.079$, $A_\lambda^V = 0.816$.

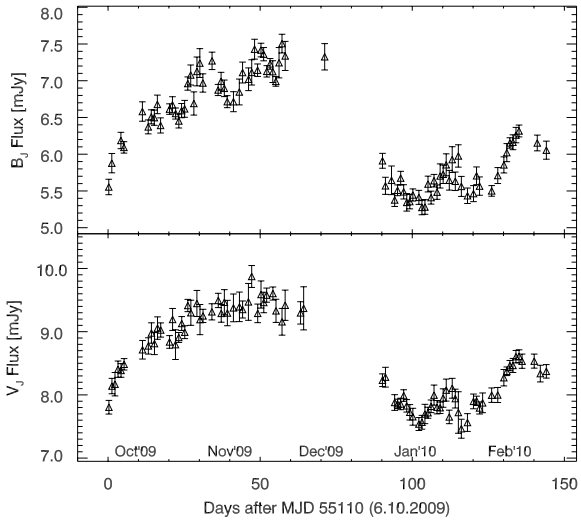

Fig. 1. Lightcurves in the 2009–2010 epoch obtained with the RoBoTT telescope. All fluxes are corrected for galactic foreground extinction.

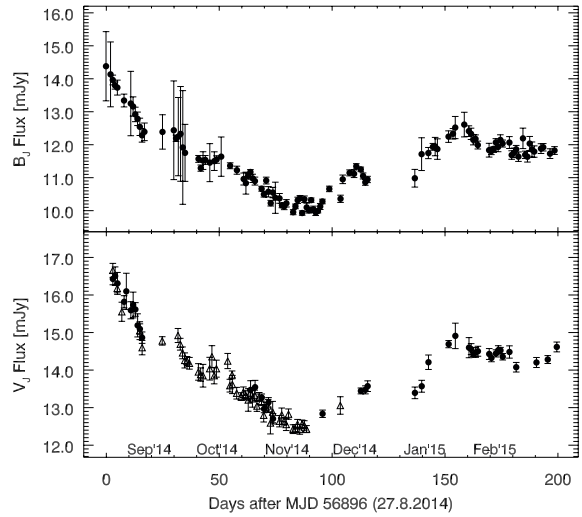

Fig. 2. Combined lightcurves in the 2014–2015 epoch, obtained with two different telescopes. Filled circles correspond to BEST II, while open triangles represent the RoBoTT observations. All fluxes are corrected for galactic foreground extinction.

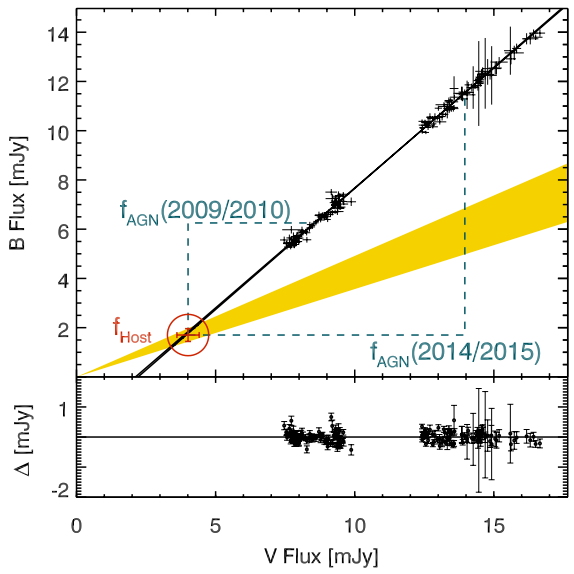

Fig. 3. B versus V flux variations of 3C 120 in the 7.″5 aperture. Each measurement is drawn as a thin cross in which the line length corresponds to the photometric uncertainties in the respective filters. The yellow filled area is the assumed host color $\Gamma_{BV,\mathrm{Host}}$, drawn to cover $B = (1.70 \pm 0.27)$ mJy and $V = (4.01 \pm 0.62)$ mJy host fluxes, as determined by Sakata et al. (2010) in an 8.″3 aperture. Our host flux estimate is the datapoint in the red circle. All data from 2009 until 2015 was used to determine the AGN slope. The black continuous line covers the upper and lower standard deviations in the AGN slope, given by the OLS bisector fit.

Table 1. Results of the FVG analysis, separated into epochs and filter sets B and V.

Epoch, filter	f_{Host}	f_{AGN}	Γ_{AGN}
	(mJy)		
2009–2015, B	1.69 ± 0.28	–	0.979 ± 0.005
2009–2015, V	3.89 ± 0.29	–	″
2009–2010, B	1.59 ± 0.26	4.66 ± 0.72	0.963 ± 0.036
2009–2010, V	3.72 ± 0.32	4.84 ± 0.76	″
2014–2015, B	1.51 ± 0.26	10.03 ± 1.08	0.959 ± 0.015
2014–2015, V	3.48 ± 0.31	10.47 ± 1.14	″

Notes. All fluxes in mJy are corrected for galactic foreground extinction as determined by Schlafly & Finkbeiner (2011). The host fluxes may also contain contributions from non-variable, narrow and broad emission lines.

our own host fluxes by measuring the center of gravity of the area that is encased by the cone of AGN slope Γ_{BV}-fitting uncertainties and Sakata's host color $\Gamma_{BV,\mathrm{Host}}$ (inside the red circle of Fig. 3). The results for the B- and V-band host fluxes (Table 1) agree well with the values of Sakata. We also fit the slopes of the individual epochs of 2009–2010 and 2014–2014 separately. For both epochs the slope is slightly flatter than the combined one, but they agree within the errors.

The offset of the combined slope (2009−2015) to the individual epoch slopes could imply that the short-term variability is redder than the long-term one. A more likely physical explanation, however, is based on the systematically different instrumental point spread functions (PSF). The PSF of the RoBoTT is slightly larger than that of the BEST II. The host also has a different spatial flux distribution at B and V. This leads to a larger host galaxy contribution in the 2009−2010 lightcurves, and the host galaxy contribution is larger in V than in B. In the net effect, compared to the 2014−2015 data, the 2009−2010 data appear slightly shifted in the FVG diagram toward the right, resulting in a marginally steeper overall Γ_{BV}. We believe that these negligible effects do not alter the basic results and conclusions on the stability of the FVG method because for all three data sets (2009−2010, 2014−2015, and 2009−2015) the host galaxy contribution is in excellent agreement within the errors. In B-band we measure a minimum $f_{B,\mathrm{AGN}} = 3.59$ mJy and a maximum of $f_{B,\mathrm{AGN}} = 12.69$ mJy. Correspondingly, the increase in V ranges from a minimum of $f_{V,\mathrm{AGN}} = 3.57$ mJy to a maximum of $f_{V,\mathrm{AGN}} = 12.76$ mJy.

3.2. Search for timescale-dependent AGN colors

The aim of this section is to investigate potential, timescale-dependent variability that has recently been observed by Sun et al. (2014) in a sample of Stripe 82 SDSS quasars. The ensemble color variability of their quasars was not constant for all observed redshifts, showing rather blue slopes on short

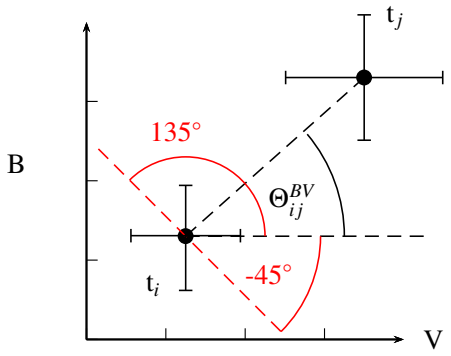

Fig. 4. Scheme of the color slope Θ_{ij}^{BV} in the B- to V-band flux plane between two measurements t_i and t_j with photometric uncertainties. If Θ falls below $-45°$ or above $135°$ we add or subtract $180°$ respectively. Restricting ourselves to the half circle, marked by the red arcs, ensures proper averaging of Θ_{ij}^{BV} for low values of τ, where photometric uncertainties dominate the slopes. A restriction to the full circle, or $-90°$ to $90°$, would bias the slope towards $0°$ if the photometric errors are large compared to the true change of flux.

timescales of <30 days that turn to redder slopes on longer timescales.

Here we improve their approach in some aspects. Instead of using magnitudes, we make use of fluxes f_ν directly. As pointed out by Kokubo et al. (2014) and references therein, fitting a straight line in magnitude–magnitude space (e.g. Sun et al. 2014) relies heavily on the contamination of the baseline flux by host galaxies and emission lines.

The color Θ_{ij}^{BV} of an arbitrary flux variation in B- and V-band in the time interval $\tau = |t_j - t_i|$ is computed using Eq. (1). The geometry is explained in Fig. 4.

$$\Theta_{ij}^{BV}(\tau) = \arctan\left(\frac{f_B(t_j) - f_B(t_i)}{f_V(t_j) - f_V(t_i)}\right). \quad (1)$$

Like Sun et al. (2014), we restrict ourselves to the range of slopes $-45° < \Theta_{ij}^{BV} < 135°$. The slopes on the other half circle represent flux decreases and are rotated by $180°$ to their equivalent slopes for a flux increase. The offset of $45°$ is chosen to equally weigh cases of both bluer (i) when brighter ($45° < \Theta_{ij}^{BV} < 135°$); and (ii) redder, when brighter ($-45° < \Theta_{ij}^{BV} < 45°$), slopes in the averaging process. The angle of $45°$ represents no color change.

Our photometric measurements in all observed epochs offer Θ_{ij}^{BV} for many combinations of t_i and t_j, with the lowest sampling interval of $\tau = 1$ day. It is useful to average all Θ_{ij}^{BV} inside bins with this size. The average of these bins is described by

$$\overline{\Theta}^{BV}(\tau) = \frac{1}{N}\sum_{ij}^{N}\Theta_{ij}^{BV}(\tau). \quad (2)$$

The results of this approach for the B- and V-band fluxes are shown in Fig. 5, together with the structure function $S(\tau)$, as defined by Eq. (3). The latter is an indicator of the strength of the variability on a specific time scale τ. The black solid lines enclose the average photometric uncertainty of each τ bin.

$$S(\tau) = \sqrt{\frac{1}{N}\sum_{ij}^{N}(f_\nu(t_j) - f_\nu(t_i))^2}. \quad (3)$$

Analyzing photometric fluxes with large uncertainties σ_i, σ_j, compared to the difference in fluxes with $|f_\nu(t_j) - f_\nu(t_i)| < \sqrt{\sigma_i^2 + \sigma_j^2}$, can cause a bias on Θ_{ij}. We assume a case of flux

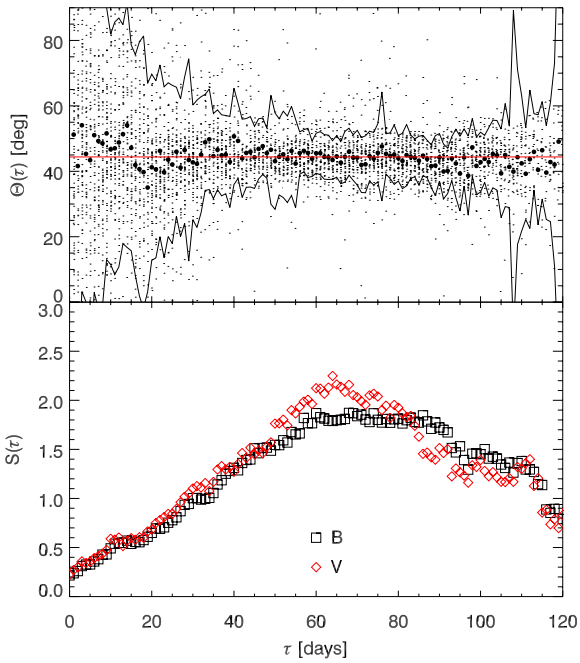

Fig. 5. *Top*: small dots represent Θ_{ij}^{BV} between all possible permutations of measurements i, j with $\tau = |t_j - t_i|$. Larger dots mark the averages inside a bin of one day with their uncertainty plotted as a continuous black line. The red straight line at $44.4°$ corresponds to the linear fit of all data $\Gamma_{BV} = 0.979$. *Bottom*: the structure function S of the variability; black boxes for B-band and red diamonds for V-band.

that is constant except for noise that is described by different photometric uncertainties for B- and V-band with $\sigma_{fB} \gg \sigma_{fV}$. Then, referring to the sketch in Fig. 4, we have $\Delta f_B \gg \Delta f_v$ for samples of measurements drawn from these distributions. As a result, we obtain $\overline{\Theta}(\tau) \approx 90°$.

The structure function $S(\tau)$ for the short timescales in Fig. 5 shows that for $\tau < 20$ days the variations are still on the order of typical photometric errors. As a consequence, the distribution of Θ_{ij}^{BV} is very broad in this region. The shape of the structure function is very similar for both bands with a slightly larger variation in amplitudes around 60 days for the V-band. For comparison purposes, we plot the previous linear fit result of $\Gamma_{BV} = 0.979$ as solid red line. In this early epoch, the majority of slopes $\overline{\Theta}^{BV}(\tau)$ is about $3°$ higher than the linear approximation but with only low significance and large scatter. From 20 to 90 days, the scatter decreases and the average cannot be distinguished from the linear fit. A potential contribution of ~5% Hβ at 25 days (Pozo Nuñez et al. 2012) may introduce additional flux to the V-band and shifts the slope downward in this region. However, there is no significant trace of this effect. After 90 days, the number of data points in the τ bins decreases naturally, causing larger scatter and a minimally lower average slope of $42°$. In summary, the plot reveals no clear difference in $\overline{\Theta}^{BV}$ on timescales τ within a single observation epoch of 3C 120.

In Fig. 6, we restrict the plot to $1640 < \tau < 1960$, so that all Θ_{ij}^{BV} have one data point in our early epoch of 2009–2010 and one in the late epoch of 2014–2015. In total, all angles $\overline{\Theta}^{BV}$ are consistent with our linear fit result, taking the photometric uncertainties into consideration. Within the errors, there appears a positive slope from $44°$ to $45°$ for the considered range of τ. This is, however, consistent with a potential host flux offset between the two epochs that originates from different PSFs as explained in Sect. 3.1.

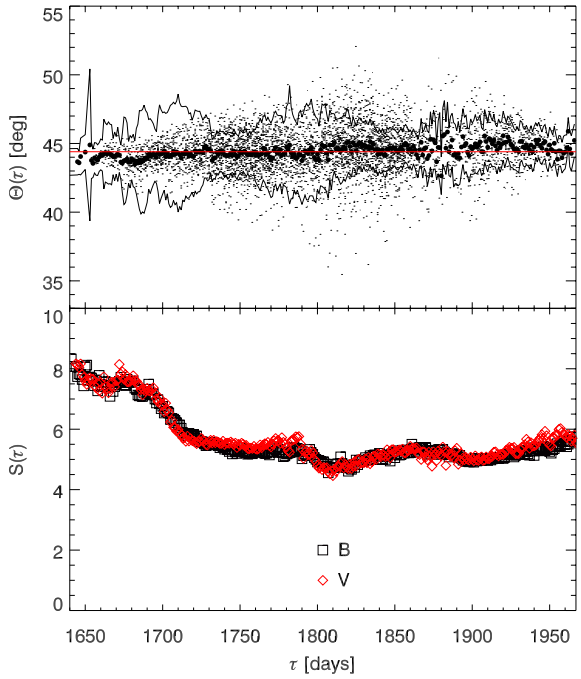

Fig. 6. Same as Fig. 5, here for the high values of τ between the epochs of 2009–2010 and 2014–2015.

4. Discussion and conclusions

Our results show a highly linear evolution of B versus V fluxes for 3C 120 on all timescales – from days to several years. Additionally, the color is highly constant, despite the AGN undergoing a strong increase of 1.4 mag in flux over a duration of five years.

Calculating their time dependent colors $\theta(\tau)$ in magnitude-magnitude space, Sun et al. (2014) report a significant change of color for g- and r-band data of a large SDSS quasar sample. The colors change from short timescale (small amplitude) blue colors to long timescale (large amplitude) red colors. Considering a total observed flux $f(t) = f_{\rm Host} + f_{\rm AGN}(t)$, composed of constant host galaxy component and variable AGN, the difference in magnitude space is

$$\Delta m_{ij}(\tau) = 2.5 \log\left(\frac{f_{\rm AGN}(t_j) + f_{\rm Host}}{f_{\rm AGN}(t_i) + f_{\rm Host}}\right). \quad (4)$$

This means that a constant host causes a reduction in the observed magnitude difference. Because the host galaxy SED is red, compared to that of the AGN, the magnitude difference will be reduced more for the red $\Delta m_r(\tau)$ compared to the blue $\Delta m_{\rm g}(\tau)$ and therefore $\theta(\tau) = \arctan(\Delta m_r(\tau)/\Delta m_{\rm g}(\tau))$ turns to artificially blue colors. Since the structure function of the SDSS quasars rises towards long timescales (Sun et al. 2014), we simultaneously observe large amplitudes of flux variations. Because the host galaxy contribution is reduced in such cases, $\theta(\tau)$ will be of a redder color. In our flux-flux approach, however, this issue is completely avoided. Therefore, we suggest that the luminosity and time-dependent color variability observed by Sun et al. is an artifact of data analysis in magnitudes instead of fluxes.

The intrinsic brightness change of any astronomical object may be caused by a change in the area and/or the temperature T of the emitting surface. While an increase in area would simply cause a constant color, the temperature change always has a degree of curvature. Only in the Rayleigh-Jeans approximation is the flux again proportional to the temperature T. Using the blue side λ of the Johnson B-band in $h\,c < \lambda\,k_B\,T$, the temperature T must be higher than 36 000 K, because it is at the lower end of typical effective AD temperatures. The existence of a linear relationship between two (optical) fluxes shows that the variable component is hot enough to be approximated by Rayleigh Jeans.

Another mechanism for a brightness change is variable extinction. In this case, the extinction law influences the color of the varying component, with the bluer band usually more affected than the red band. As a result, extinction can provide a different color slope than a temperature fluctuation in the AD. However, extinction variations resulting from dust clouds that move into the line of sight are random events and should occur with diverse amplitude and timescales. Because they are independent of the variations in the AD with different its color, nonlinear behavior of the total fluxes should then be observed in individual objects. Averaging a large sample of AGN flux variations, such random disturbances of the slope in the flux-flux diagrams will be washed out.

Our results are consistent with variations that stem from temperature changes in the AD, where the B- and V-bands are placed in the Rayleigh-Jeans tail of the thermal emission. There is no evidence for a short timescale, bluer color variation that may be caused by variable extinction in the line of sight.

In summary, our finding makes a good case for the use of the rest-frame optical FVG method on different timescales of low luminosity AGN. To further confirm this result, more longterm observations of varying Seyferts (and also quasars) with high photometric precision and dense (daily) temporal sampling will be required.

Acknowledgements. This research made use of the NASA/IPAC Extragalactic Database (NED) which is operated by the Jet Propulsion Laboratory, California Institute of Technology, under contract with the National Aeronautics and Space Administration (NASA). This publication is supported as a project of the Nordrhein-Westfälische Akademie der Wissenschaften und der Künste, in the framework of the academy program of the Federal Republic of Germany and the state of Nordrhein-Westfalen. This work is supported by the DFG Program (HA 3555/12-1). The observations on Cerro Armazones benefited from the support of guardians, Hector Labra, Gerardo Pino, Roberto Munoz, and Francisco Arraya. We thank the referee, Ian Glass, for his helpful comments and careful review of the manuscript.

References

Choloniewski, J. 1981, Acta Astron., 31, 293
Giveon, U., Maoz, D., Kaspi, S., Netzer, H., & Smith, P. S. 1999, MNRAS, 306, 637
Kabath, P., Erikson, A., Rauer, H., et al. 2009, A&A, 506, 569
Kokubo, M., Morokuma, T., Minezaki, T., et al. 2014, ApJ, 783, 46
Meusinger, H., Hinze, A., & de Hoon, A. 2011, A&A, 525, A37
Paltani, S., & Walter, R. 1996, A&A, 312, 55
Pozo Nuñez, F., Ramolla, M., Westhues, C., et al. 2012, A&A, 545, A84
Sakata, Y., Minezaki, T., Yoshii, Y., et al. 2010, ApJ, 711, 461
Sakata, Y., Morokuma, T., Minezaki, T., et al. 2011, ApJ, 731, 50
Schlafly, E. F., & Finkbeiner, D. P. 2011, ApJ, 737, 103
Sun, Y.-H., Wang, J.-X., Chen, X.-Y., & Zheng, Z.-Y. 2014, ApJ, 792, 54
Wamsteker, W., Rodriguez-Pascual, P., Wills, B. J., et al. 1990, ApJ, 354, 446
Webb, W., & Malkan, M. 2000, ApJ, 540, 652
Wilhite, B. C., Vanden Berk, D. E., Kron, R. G., et al. 2005, ApJ, 633, 638
Winkler, H. 1997, MNRAS, 292, 273
Winkler, H., Glass, I. S., van Wyk, F., et al. 1992, MNRAS, 257, 659

Appendix A: Measured fluxes

Table A.1. Galactic foreground extinction corrected *B*-band fluxes from 2009 until 2015.

MJD	Flux	Error
days	mJy	
55 110.237	5.55421	0.105191
55 111.234	5.8784	0.131488
55 114.225	6.18674	0.111323
55 115.223	6.09283	0.077608
55 121.283	6.58088	0.132027
55 123.203	6.37179	0.0947509
55 124.209	6.5088	0.0957203
55 125.209	6.49741	0.103942
55 126.209	6.67802	0.126342
55 127.264	6.39158	0.103038
55 130.204	6.61423	0.0713771
55 131.166	6.67221	0.110278
55 132.208	6.55387	0.075334
55 133.260	6.45186	0.0950582
55 134.166	6.59332	0.0966424
55 135.172	6.61771	0.114972
55 136.209	6.96171	0.0903407
55 137.175	7.07786	0.136614
55 138.209	6.69046	0.158005
55 139.218	7.12651	0.196419
55 140.175	7.24073	0.196107
55 141.175	6.96943	0.124644
55 144.185	7.27056	0.118578
55 146.175	6.874	0.0758508
55 147.153	6.99352	0.121185
55 148.216	6.89657	0.112869
55 149.175	6.71507	0.0817101
55 151.222	6.71472	0.136257
55 153.145	6.84699	0.175694
55 154.217	7.11164	0.142083
55 156.181	7.02015	0.15446
55 157.226	7.11348	0.171963
55 158.164	7.42939	0.135409
55 159.148	7.14331	0.085071
55 160.268	7.41794	0.0926098
55 161.144	7.36146	0.0904423
55 162.188	7.12791	0.0774404
55 163.262	7.22946	0.0724561
55 164.148	7.12385	0.148103
55 165.159	6.99121	0.065618
55 166.200	7.24529	0.206256
55 167.177	7.50535	0.127324
55 168.226	7.3375	0.197946
55 181.213	7.32589	0.179363
55 200.209	5.91065	0.101208
55 201.179	5.57005	0.116409
55 203.179	5.64471	0.194746
55 204.216	5.37734	0.088279
55 205.160	5.50883	0.0735336
55 206.194	5.67506	0.0920804
55 207.180	5.48779	0.0972899
55 208.188	5.34417	0.118273
55 209.185	5.35524	0.0988943
55 210.200	5.44533	0.0826862
55 212.181	5.41264	0.095357
55 213.176	5.27572	0.0994904
55 214.169	5.28162	0.0990277
55 215.171	5.59415	0.107598
55 216.185	5.40936	0.0881853
55 217.145	5.6395	0.0854541
55 218.158	5.48408	0.0979306
55 219.161	5.70425	0.164234
55 220.156	5.72685	0.125466
55 221.153	5.8559	0.149499
55 222.168	5.64563	0.134439
55 223.128	5.92687	0.175566
55 224.146	5.63153	0.125795
55 225.142	5.97617	0.152117
55 226.138	5.56186	0.13634
55 228.152	5.43482	0.105249
55 230.126	5.4637	0.10911
55 231.127	5.70627	0.120521
55 232.122	5.56605	0.124716
55 236.111	5.50081	0.0723353
55 238.111	5.70972	0.108597
55 240.117	5.85487	0.10974
55 241.081	6.02139	0.122924
55 242.096	6.15323	0.0706417
55 243.097	6.16286	0.101422
55 244.087	6.26022	0.104736
55 245.096	6.31632	0.0806359
55 251.089	6.15306	0.107161
55 254.081	6.05505	0.123017
56 895.368	14.3804	1.04936
56 897.366	14.1336	0.983937
56 898.358	13.9633	0.147968
56 899.358	13.7959	0.109101
56 900.385	13.7324	0.226593
56 903.344	13.3408	0.194499
56 906.327	13.2489	0.976908
56 907.343	13.1597	0.291964
56 908.330	12.9185	0.220106
56 909.325	12.7856	0.204544
56 910.333	12.5424	0.262686
56 911.312	12.2846	0.206587
56 912.377	12.3907	0.266982
56 920.377	12.3876	0.521437
56 925.375	12.4381	1.49668
56 926.373	12.1945	0.0961339
56 927.369	12.2455	1.18698
56 928.367	12.3288	1.43678
56 929.364	11.9162	1.7241
56 930.361	11.7529	0.864746
56 936.336	11.5692	0.10415
56 937.335	11.29	0.0942527
56 938.334	11.5188	0.268483
56 939.334	11.5381	0.133113
56 941.330	11.4562	0.576352
56 943.325	11.5018	0.283021
56 944.352	11.5507	0.11299
56 946.374	11.6383	0.596045
56 950.347	11.3615	0.0897234
56 953.332	11.2265	0.121999
56 956.323	10.9593	0.181796
56 957.321	10.8346	0.332822
56 958.321	11.0549	0.0997387
56 959.313	11.1725	0.0734273
56 960.311	10.9795	0.125564
56 961.314	10.8968	0.120839
56 964.273	10.665	0.0736191
56 965.272	10.496	0.084032
56 966.310	10.913	0.103403
56 967.265	10.5722	0.156577
56 968.306	10.2267	0.0856314
56 969.261	10.5487	0.157831
56 970.352	10.391	0.472495
56 972.202	10.3721	0.148061
56 973.287	10.1588	0.0703249
56 974.284	10.1296	0.0993075

Table A.1. continued.

MJD	Flux	Error
days	mJy	
56 975.258	10.2233	0.112217
56 978.251	9.95252	0.0759752
56 979.248	10.129	0.0708522
56 980.246	10.3133	0.0943685
56 981.243	10.3805	0.0763472
56 982.240	9.92794	0.066818
56 983.237	10.3451	0.0996063
56 984.235	10.098	0.130562
56 985.231	10.0103	0.0832779
56 986.222	10.3187	0.0663072
56 987.215	10.0418	0.095233
56 988.211	9.94455	0.0923461
56 989.211	9.98914	0.0576447
56 990.230	10.1267	0.0918454
56 991.199	10.2779	0.0700807
56 994.243	10.6593	0.083241
56 999.226	10.3593	0.109408
57 000.196	10.9499	0.13015
57 003.220	11.1454	0.090543
57 005.216	11.1176	0.114169
57 006.198	11.3441	0.0799838
57 008.191	11.2517	0.069811
57 009.205	11.0519	0.0910484
57 010.192	10.8618	0.0919861
57 011.188	10.946	0.0958581
57 032.126	10.9831	0.268319
57 035.126	11.7138	0.496919
57 038.123	11.7465	0.169581
57 040.123	11.9359	0.102771
57 041.122	11.9438	0.278621
57 042.122	11.8676	0.310776
57 047.059	12.2454	0.174759
57 049.023	12.3322	0.15833
57 050.022	12.5201	0.336703
57 054.020	12.6104	0.374115
57 056.067	12.4112	0.161701
57 057.020	12.3306	0.171476
57 058.020	12.1477	0.15279
57 059.019	12.1763	0.122279
57 060.019	11.9898	0.11905
57 065.016	11.8339	0.208689
57 066.016	11.8045	0.104941
57 067.052	11.8566	0.0844698
57 068.014	12.0699	0.114009
57 069.014	11.9332	0.14584
57 070.013	12.1462	0.155033
57 071.013	12.0355	0.106119
57 074.011	12.0657	0.180716
57 075.010	11.6865	0.129328
57 076.010	11.7541	0.144578
57 077.009	11.861	0.11675
57 078.008	11.6374	0.143872
57 080.008	12.1926	0.310672
57 081.007	11.6933	0.112834
57 082.006	11.6342	0.160317
57 083.005	12.0345	0.216004
57 084.004	11.8517	0.231508
57 085.004	11.7921	0.172509
57 088.002	11.8821	0.148556
57 089.002	11.9226	0.112329
57 092.004	11.7295	0.147702
57 093.997	11.8236	0.117837

Table A.2. Galactic foreground extinction corrected V-band fluxes from 2009 until 2015.

MJD	Flux	Error
days	mJy	
55 110.283	7.80492	0.107975
55 111.280	8.13988	0.122128
55 112.281	8.16902	0.185274
55 113.274	8.40669	0.129154
55 114.271	8.38676	0.107963
55 115.269	8.48413	0.0902408
55 121.329	8.71428	0.14702
55 123.249	8.77489	0.128866
55 124.255	8.97913	0.161263
55 125.255	8.8118	0.174615
55 126.255	9.05692	0.177551
55 127.311	9.02664	0.112698
55 130.215	8.83791	0.100329
55 131.213	9.19359	0.173977
55 132.161	8.79508	0.234881
55 133.248	8.90878	0.0787138
55 134.213	9.12944	0.109715
55 135.219	8.99221	0.101696
55 136.219	9.41409	0.0970858
55 137.222	9.29944	0.19867
55 139.208	9.44626	0.206467
55 140.222	9.19151	0.238798
55 141.221	9.24981	0.104757
55 144.138	9.31401	0.1281
55 146.223	9.49443	0.113287
55 147.199	9.28943	0.139888
55 148.227	9.46577	0.199261
55 149.223	9.2952	0.201076
55 151.211	9.37694	0.219707
55 153.192	9.39334	0.233614
55 154.228	9.35126	0.134791
55 156.135	9.47155	0.291827
55 157.216	9.87356	0.173444
55 159.196	9.29006	0.147111
55 160.280	9.58813	0.214793
55 161.192	9.46201	0.161921
55 162.139	9.57828	0.112009
55 164.196	9.60405	0.103562
55 165.207	9.32988	0.183195
55 167.188	9.15643	0.211352
55 168.214	9.41859	0.239692
55 173.276	9.29753	0.176752
55 174.295	9.36956	0.341082
55 200.199	8.23195	0.100521
55 201.189	8.28018	0.156595
55 204.206	7.87946	0.124108
55 205.170	7.85903	0.0732903
55 206.184	7.8568	0.0907966
55 207.190	7.9896	0.0916827
55 208.178	7.82703	0.0989102
55 209.196	7.72464	0.122169
55 210.190	7.65428	0.133864
55 212.170	7.53899	0.102164
55 213.186	7.56678	0.109318
55 214.159	7.698 0	.152955
55 215.181	7.71733	0.0871391
55 216.174	7.81947	0.0996844
55 217.155	7.99646	0.159476
55 218.148	7.80512	0.105828
55 219.171	7.79658	0.0913465
55 220.146	7.95024	0.146176
55 221.164	8.0759	0.174263
55 222.158	7.65141	0.107348
55 223.138	8.10472	0.157151
55 224.136	7.94129	0.148864

Table A.2. continued.

MJD	Flux	Error
days	mJy	
55 225.153	7.72148	0.328673
55 226.128	7.46477	0.150035
55 228.142	7.56282	0.140573
55 230.116	7.89702	0.116355
55 231.137	7.90614	0.0739646
55 232.112	7.79313	0.0957212
55 233.130	7.87441	0.156332
55 236.101	7.99585	0.114276
55 238.101	7.99872	0.119167
55 240.107	8.27189	0.130001
55 241.091	8.37387	0.0684091
55 242.085	8.46378	0.0811344
55 243.107	8.46584	0.1109
55 244.077	8.60484	0.0984047
55 245.107	8.61162	0.10168
55 246.096	8.53311	0.112621
55 250.085	8.53457	0.111314
55 252.090	8.33699	0.131954
55 254.071	8.37249	0.106794
56 898.378	16.6557	0.186138
56 900.322	16.1771	0.120272
56 902.367	15.5529	0.254201
56 910.310	15.0494	0.238098
56 911.354	14.5983	0.191545
56 920.261	14.7768	0.112215
56 927.240	14.9211	0.186894
56 928.240	14.6891	0.156857
56 929.240	14.4583	0.157344
56 930.230	14.2573	0.200672
56 931.262	14.2388	0.121795
56 932.304	14.1808	0.155984
56 936.268	13.9515	0.220356
56 937.268	13.8814	0.177064
56 938.323	13.8499	0.301957
56 941.267	14.0377	0.302282
56 942.268	14.3559	0.294361
56 943.261	13.8518	0.218258
56 944.261	14.0379	0.226156
56 949.247	14.2412	0.20211
56 950.210	13.5852	0.169376
56 951.199	13.8724	0.104292
56 951.308	13.6163	0.242234
56 953.227	13.3842	0.155249
56 955.206	13.2942	0.103009
56 956.206	13.4105	0.140081
56 957.206	13.3262	0.122764
56 958.342	13.2041	0.300121
56 959.205	13.3902	0.108892
56 960.206	13.2339	0.221935
56 961.206	13.323	0.142973
56 962.206	13.0426	0.14191
56 963.220	13.288	0.11486
56 964.205	13.1691	0.11433
56 965.192	12.7974	0.180278
56 966.192	13.0069	0.130979
56 967.175	13.0466	0.172496
56 968.175	12.5915	0.292129
56 969.175	12.8817	0.28501
56 972.175	12.6383	0.150737
56 973.175	12.8066	0.183076
56 974.174	12.6368	0.101455
56 975.174	12.5512	0.160767
56 976.184	12.8272	0.137709
56 978.177	12.4271	0.117361
56 979.175	12.4385	0.110956
56 980.172	12.5612	0.125104

Table A.2. continued.

MJD	Flux	Error
days	mJy	
56 981.169	12.4201	0.128426
56 982.166	12.5571	0.112808
56 983.163	12.5241	0.127495
56 984.160	12.4284	0.0935889
56 999.121	13.0574	0.232812
57 013.083	13.0503	0.157684
56 898.394	16.4276	0.155995
56 899.395	16.5029	0.245028
56 900.422	16.3084	0.292189
56 903.380	15.8189	0.162293
56 904.354	16.0975	0.481578
56 906.363	15.5928	0.227986
56 907.379	15.7337	0.342789
56 908.366	15.6151	0.180709
56 909.360	15.1909	0.30776
56 910.369	15.0948	0.136874
56 911.348	14.8637	0.152151
56 959.379	13.4723	0.244766
56 961.380	13.5448	0.18189
56 964.338	13.268	0.095813
56 965.338	12.9671	0.103183
56 967.330	13.1403	0.127211
56 969.326	12.7035	0.139011
56 991.264	12.8366	0.0982572
57 008.240	13.4449	0.0784246
57 010.241	13.4736	0.106579
57 011.237	13.5716	0.142467
57 032.176	13.3936	0.154944
57 035.177	13.5697	0.15817
57 038.172	14.2091	0.192206
57 047.108	14.6907	0.0955832
57 050.073	14.9109	0.339064
57 056.117	14.5971	0.267836
57 057.070	14.5593	0.145233
57 058.070	14.4118	0.0502472
57 059.069	14.4694	0.130669
57 060.069	14.5013	0.132637
57 065.069	14.4286	0.145172
57 066.066	14.3239	0.101617
57 068.065	14.4446	0.0949995
57 069.064	14.5274	0.121463
57 070.064	14.5247	0.0796847
57 071.063	14.3549	0.0858158
57 074.037	14.4823	0.16363
57 077.034	14.0762	0.127564
57 086.003	14.2022	0.133571
57 091.003	14.2806	0.105551
57 093.997	14.616	0.131274